Chinese Chemical Letters 36 (2025) 110119

Contents lists available at ScienceDirect

Chinese Chemical Letters

journal homepage: www.elsevier.com/locate/cclet

Ratiometric NIR-II fluorescent organic nanoprobe for imaging and monitoring tumor-activated photodynamic therapy

Baoli Yin[a], Xinlin Liu[a], Zhe Li[a], Zhifei Ye[a], Youjuan Wang[a], Xia Yin[a,*], Sulai Liu[b,*], Guosheng Song[a], Shuangyan Huan[a,*], Xiao-Bing Zhang[a]

[a] State Key Laboratory of Chemo/Biosensing and Chemometrics, College of Chemistry and Chemical Engineering, Hunan University, Changsha 410082, China
[b] Department of Hepatobiliary Surgery, Hunan Provincial People's Hospital/The First Affiliated Hospital of Hunan Normal University, Changsha 410082, China

ARTICLE INFO

Article history:
Received 20 March 2024
Revised 11 June 2024
Accepted 12 June 2024
Available online 13 June 2024

Keywords:
Photodynamic therapy
Ratiometric
NIR-II fluorescent
Nanoprobe
Image-guided therapy

ABSTRACT

Photodynamic therapy (PDT) has emerged as a promising approach for tumor treatment due to its non-invasiveness and high selectivity. However, the off-target activation of phototoxicity and the limited availability of tumor-specific biomarkers pose challenges for effective PDT. Here, we present the development of a novel ratiometric near-infrared-II (NIR-II) fluorescent organic nanoprobe, BTz-IC@IR1061, which responds specifically to hypochlorite (HClO) within tumors. This nanoprobe allows ratiometric fluorescence imaging to monitor and guide activated tumor PDT. BTz-IC@IR1061 nanoparticles were synthesized by codoping the small molecule dye BTz-IC, which generates reactive oxygen species (ROS), with the commercial dye IR1061. The presence of HClO selectively activates the fluorescence and photodynamic properties of BTz-IC while destroying IR1061, enabling controlled release of ROS for tumor therapy. We demonstrated the high selectivity of the nanoprobe for HClO, as well as its excellent photostability, photoacoustic imaging capability, and photothermal effects. Furthermore, *in vivo* studies revealed effective tumor targeting and remarkable tumor growth inhibition through tumor-activated PDT. Our findings highlight the potential of BTz-IC@IR1061 as a promising tool for tumor-specific PDT, providing new opportunities for precise and controlled cancer therapy.

Photodynamic therapy (PDT) is an approved clinical treatment for various cancers, including cholangiocarcinoma, oral cancer, and pancreatic cancer [1-5]. PDT involves reactions between photosensitizers and endogenous oxygen, resulting in the production of highly cytotoxic reactive oxygen species (ROS) that eliminate cancer cells and associated tissues [6-8]. In comparison to traditional treatments like chemotherapy and radiation therapy, PDT offers advantages such as non-invasiveness, minimal side effects, and excellent spatiotemporal selectivity [8-10]. Consequently, PDT has garnered significant attention as a promising approach to tumor treatment [11]. By focusing light on specific tumor areas, PDT can limit induced damage to selectively target tissues. However, patients must remain in darkness for an extended period after undergoing PDT to expel photosensitizers from their bodies and prevent unnecessary damage to the skin or normal tissues [12,13]. Therefore, achieving specific therapy in tumor PDT remains a key research focus.

Several tumor-targeting ligands, such as peptides, adaptors, and biotins, have been developed to enhance the specific enrichment of photosensitizers in tumors [14-16]. Although this strategy promotes the uptake of cancer cells, the continuous presence of these ligands may lead to phototoxicity at non-target locations. To address this issue, activatable photosensitizers have been developed in recent years. These photosensitizers are activated by highly expressed stimuli within tumors [17-20]. In the absence of tumor-related stimuli, even in the presence of a light source, the photosensitizer remains in a passive state. However, when stimuli are present, the photosensitizer's photosensitivity is activated, facilitating controlled release of ROS under light conditions while minimizing damage to normal tissues. Currently, several tumor-related biomarker activated photosensitizers, such as β-galactosidase and cathepsin, have been developed [21-23]. However, due to the minimal difference in expression levels between cancer cells and normal cells, off-target activation of phototoxicity often occurs, resulting in unpredictable side effects [24]. Consequently, there is an urgent need to develop photosensitizers activated by alternative tumor-related biomarkers.

* Corresponding authors.
E-mail addresses: yinxia@hnu.edu.cn (X. Yin), liusulai@hunnu.edu.cn (S. Liu), syhuan@hnu.edu.cn (S. Huan).

https://doi.org/10.1016/j.cclet.2024.110119
1001-8417/

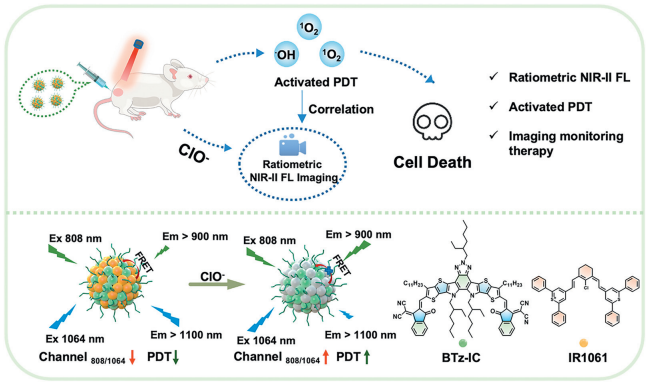

Scheme 1. Schematic illustration of ratiometric NIR-II FL imaging guided activated PDT cancer therapy.

Neutrophils, as part of the body's defense against tumors and invasive pathogens, play a crucial role in clearing tumors and infections [25-27]. They generate large amounts of ROS by promoting the expression of myeloperoxidase (MPO) [27]. Notably, the infiltration of neutrophils during acute inflammation can increase local ROS levels up to 20 times, leading to tumor cell death [28,29]. Hypochlorite (HClO) production, accomplished through the catalytic action mediated by MPO, serves as one of the most potent effectors [30]. Therefore, effective recruitment of neutrophils to inflammatory sites is crucial for producing highly reactive HClO for antitumor and antibacterial purposes. Inflammation is typically accompanied by an upregulation of hydrogen peroxide (H_2O_2) levels [31]. Endogenous neutrophils catalyze the conversion of excess H_2O_2 into locally restricted and highly active HClO during inflammation, specifically killing pathogens and reducing H_2O_2-related damage [32]. However, insufficient neutrophil recruitment and low catalytic activity hinder their biomedical applications. Thus, developing methods to increase neutrophil numbers and enhance their catalytic activity is necessary to enhance HClO-mediated antitumor effects.

In this study, we developed a novel ratiometric near-infrared-II (NIR-II) fluorescent (FL) organic nanoprobe (BTz-IC@IR1061) that responds to HClO within tumors (Scheme 1). This nanoprobe achieves ratiometric FL changes and PDT activation, with the activation of PDT being monitored through ratiometric NIR-II FL changes. The nanoprobe consists of two main components. The first component is the organic small molecule dye BTz-IC, which extends the conjugated system to achieve NIR-II FL emission by introducing two receptor groups at both ends of the traditional donor-receptor-donor (D-A'-D) core. Under light irradiation, the BTz-IC molecule generates hydroxyl radical (·OH) and singlet oxygen ($^1O_2$) through type I and type II photodynamic processes. The second component is the commercial cyanine dye IR1061. The fluorescence resonance energy transfer (FRET) was observed between the two molecules when they were co-doping. In addition, the photodynamic properties of BTz-IC were quenched as well. Incubation with HClO restored the fluorescence and photodynamic property of BTz-IC molecules while destroying IR1061. After PDT, inflammation occurred at the tumor site, which led to infiltration of neutrophils within the tumor, with an increase in HClO concentration, further leading to the destruction of IR1061 and the activation of ratio fluorescence and PDT in tumor. Finally, the ratiometric NIR-II fluorescence probe can monitor the activated tumor PDT process.

The BTz-IC molecule was synthesized as previously reported method (Fig. 1a). Confirmation of successful synthesis was achieved through ^1H nuclear magnetic resonance (NMR) and matrix-assisted laser desorption ionization time-of-flight mass spectrometry (MALDI-TOF MS) techniques (Figs. S1 and S2 in

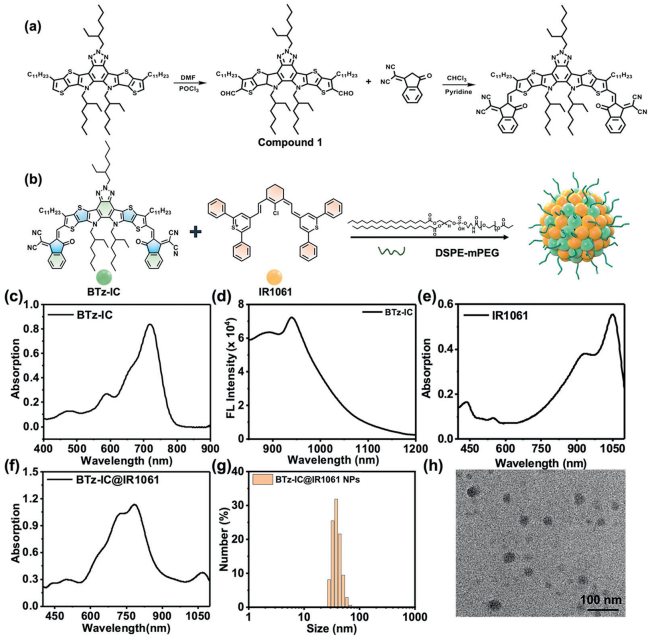

Fig. 1. (a) The synthetic route of BTz-IC molecule. (b) Schematic diagram of the synthesis of BTz-IC@IR061 nanoparticles. (c) The ultraviolet absorption spectrum of BTz-IC molecule in tetrahydrofuran (THF). (d) The fluorescence spectrum of BTz-IC molecule in THF. (e) The UV absorption spectrum of IR1061 molecule in THF. (f) The ultraviolet absorption spectrum of BTz-IC@IR1061 NPs (in H_2O). (g) The DLS of BTz-IC@IR1061 NPs. (h) TEM of BTz-IC@IR1061 NPs.

Supporting information). Ultraviolet and visible spectrophotometry (UV–vis) absorption spectra demonstrated a characteristic absorption peak at 730 nm for the BTz-IC molecule (Fig. 1c). Additionally, fluorescence spectra revealed strong emission ranging from 850 nm to 1100 nm for the BTz-IC molecule (Fig. 1d). Moreover, the absorption spectrum of IR1061 ranged from 800 nm to 1100 nm, overlapping with the fluorescence emission range of BTz-IC (Fig. 1e). Consequently, FRET between the two molecules could quench the fluorescence of BTz-IC. To further investigate, we assembled these two small organic molecules into nanoparticles using the surfactant 1,2-dimyristoyl-*sn*–glycero-3-phospho-ethanolamine-*N*-[methoxy(poly(ethylene glycol)] (DSPE-mPEG) (Fig. 1b).

To optimize the FRET effectiveness, we systematically screened the doping ratio of the two molecules within the nanoprobe. With a fixed mass of surfactant DSPE-mPEG (25 mg), we synthesized nanoprobes (BTz-IC@IR1061) with various doping ratios of BTz-IC and IR1061, namely 1:1, 1:2, 2:1, 5:3, and 3:5. We examined the changes in ultraviolet spectra before and after the addition of ClO^-. As depicted in Fig. 1f and Fig. S3 (Supporting information), nanoprobes with different doping ratios exhibited both of the characteristic absorption peaks of BTz-IC and IR1061, indicating successful doping. Subsequently, the absorption at 1064 nm of 5:3, 2:1, and 1:1 nanoprobes decreased after the addition of ClO^-, while the absorption at 808 nm remained unchanged. This result signified the destruction of IR1061 while the reference molecule BTz-IC exhibited no reactivity to ClO^-. Conversely, the doping levels of IR1061 within the 3:5 and 1:2 groups were too high, leading to IR1061 aggregation and significant absorption blue shift. This undesirable outcome impeded the ClO^- response. Consequently, the ratio of 5:3 was selected for further exploration.

Once the doping ratio of the two organic small molecules was determined, we synthesized the nanoprobe using the final ratio and characterized its morphology. Transmission electron microscopy (TEM) images of BTz-IC@IR1061 demonstrated symmet-

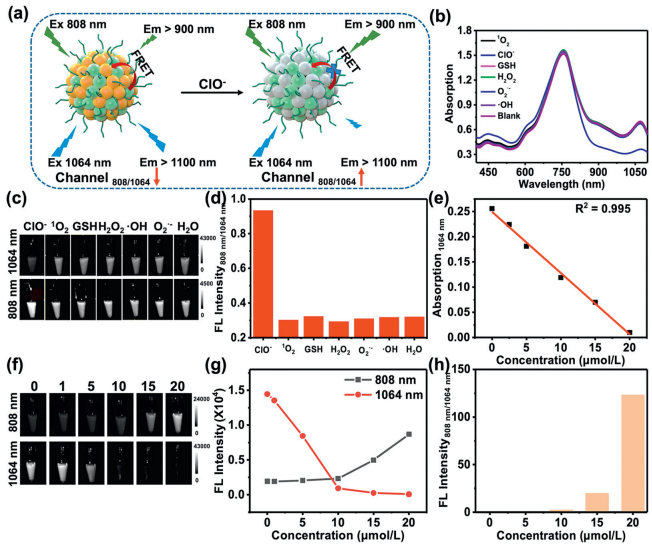

Fig. 2. (a) Schematic diagram of ClO^- response ratiometric fluorescence changes. (b) UV spectrum changes of BTz-IC@IR1061 nanoparticles incubated with different ROS (GSH, H_2O_2, $^1O_2$, $O_2^{\cdot-}$, ·OH, ClO^-. The final concentration was 50 μmol/L). (c) Changes of fluorescence images of BTz-IC@IR1061 nanoparticles incubated with different ROS (GSH, H_2O_2, $^1O_2$, $O_2^{\cdot-}$, ·OH, ClO^-. The final concentration was 50 μmol/L). (d) Changes in fluorescence ratio of 808 nm/1064 nm of BTz-IC@IR1061 nanoparticles incubated with different ROS. (e) Ultraviolet absorption spectra at 1064 nm of BTz-IC@IR1061 nanoparticles reacting with different concentrations of ClO^- (0, 2.5, 5, 10, 15, 20 μmol/L). (f) Changes of fluorescence images in the NIR-II in different channels after the reaction of BTz-IC@IR1061 nanoparticles with different concentrations of ClO^- (0, 5, 7.5, 10, 12.5, 15, 20 μmol/L; Ex: 808 nm, Em > 900 nm; Ex: 1064 nm, Em > 1100 nm). (g) Changes of fluorescence values in two channels after the reaction of BTz-IC@IR1061 nanoparticles with different concentrations of ClO^-. (h) Fluorescence ratios of BTz-IC@IR1061 nanoparticles reacting with different concentrations of ClO^- (808 nm/1064 nm).

rical spherical nanoparticles with a size of 31 nm (Fig. 1h). Furthermore, BTz-IC@IR1061 nanoparticles exhibited high water solubility with a dynamic light scattering (DLS) size of approximately 38 nm (Fig. 1g). The TEM and DLS sizes were in good agreement. At the same time, the size of the BTz-IC@IR1061 did not change significantly in different solvents (H_2O, 1640 cell culture medium, phosphate buffer saline (PBS)) at different times, indicating that the particles had good stability (Fig. S4 in Supporting information). Moreover, the zeta potential measured −25.1 mV (Fig. S5 in Supporting information).

By co-doping the two molecules with surfactants to synthesize BTz-IC@IR1061 nanoparticles, a FRET occurred, quenching the fluorescence and photodynamic properties of BTz-IC molecules. Upon incubation with ClO^-, IR1061 was destroyed, there-by restoring the fluorescence and photodynamic properties of BTz-IC molecules (Fig. 2a). To validate the specific response of the nanoprobe to ClO^-, we conducted a study on the probe's selectivity. Based on relevant literature, we selected several common and highly expressed analytical substrates in tumors, namely glutathione (GSH), H_2O_2, $^1O_2$, $O_2^{\cdot-}$, ·OH, and ClO^-. The nanoprobes were individually incubated with these analytes, and their UV spectra were analyzed to observe any changes. As shown in Fig. 2b, the absorption at 1064 nm exhibited negligible change upon addition of the other substrates (GSH, H_2O_2, $^1O_2$, $O_2^{\cdot-}$, ·OH). In contrast, the absorption at 1064 nm significantly decreased with the addition of ClO^-. In addition, we tested the particle size of the nanoparticles before and after the ClO^- response. As shown in Fig. S6 (Supporting information), the size of the nanoparticles did not change after the ClO^- response, effectively suggesting destruction of IR1061. Furthermore, we investigated selectivity through NIR-II fluorescence, as illustrated in Fig. 2c. After sufficient reaction with GSH, H_2O_2, $^1O_2$, $O_2^{\cdot-}$, and ·OH, the fluorescence at 808 nm and 1064 nm remained unaltered. Conversely, upon reaction with ClO^-, the fluorescence at 808 nm increased while the fluorescence at 1064 nm diminished due to the cessation of FRET caused by the destruction of IR1061. Additionally, calculating the fluorescence ratio at 808 nm/1064 nm before and after the reaction to different ROS revealed that the fluorescence ratio following the addition of ClO^- was 0.94, whereas the ratios for GSH, H_2O_2, $^1O_2$, $O_2^{\cdot-}$, ·OH, and water were 0.32, 0.29, 0.30 0.31, 0.32, and 0.32, respectively. In summary, BTz-IC@IR1061 displayed high selectivity exclusively for ClO^- (Fig. 2d).

After studying the selectivity of nanoprobes, we proceeded to validate the reaction of BTz-IC@IR1061 nanoparticles with various concentrations of ClO^-. The nanoprobe was subjected to different concentrations of ClO^- and measured for absorption and fluorescence. Fig. S7 (Supporting information) revealed that as the concentration of ClO^- increased, the absorption at 808 nm remained constant, while the absorption at 1064 nm gradually decreased. This trend indicated that although the internal reference molecule BTz-IC remained unaffected, IR1061 was gradually destroyed. The detection limit of ClO^- was determined to be 0.62 μmol/L (Fig. 2e). Additionally, as displayed in Figs. 2f and g, the fluorescence under 808 nm excitation increased while the fluorescence under 1064 nm excitation decreased with increasing concentrations of ClO^-. Calculating the fluorescence ratio of 808 nm/1064 nm in response to varying ClO^- concentrations revealed a ratio as high as 123.25 at a ClO^- concentration of 20 μmol/L, whereas the ratio was 0.13 at a ClO^- concentration of 0 μmol/L (Fig. 2h). In conclusion, the probe displayed excellent detection performance for ClO^- and exhibited potential for *in vivo* research.

According to the above results, ClO^- can activate the ratiometric fluorescence of BTz-IC@IR1061 nanoprobes. Next, we studied the properties of the photodynamic therapy of BTz-IC@IR1061 nanoparticles activated by ClO^- to verify whether the activation of photodynamic therapy can be monitored by ratiometric fluorescence (Fig. 3a). The activation of PDT was validated by reacting different concentrations of ClO^- with a 5:3 ratio of BTz-IC to IR1061 (Figs. 3b and c, and Fig. S8 in Supporting information). Upon 808 nm laser illumination for 30 s, the absorption of 1,3-diphenylisobenzofuran (DPBF) at 415 nm decreases significantly with increasing ClO^- concentration. This result was attributed to the more severe damage to FRET between the nanoprobes as the ClO^- concentration increased, leading to enhanced photodynamic recovery of the BTz-IC molecule. Additionally, the ratio of absorption (A_t) at 415 nm after 30 s of illumination to absorption (A_0) before illumination (A_t/A_0) was calculated (Fig. 3d). At a ClO^- concentration of 20 μmol/L, the ratio was 0.591, while at 0 μmol/L ClO^-, the ratio was 0.879, indicating full activation of PDT after the ClO^- reaction.

Based on the absorption changes of ROS detected by DPBF, even under extremely low laser irradiation conditions (0.1 W/cm^2) for 10 s, the peak at 415 nm sharply decreased. This observation suggested that a large amount of ROS was generated during the PDT process of the molecule, capable of generating both free radicals such as ·OH through type I photodynamic processes and $^1O_2$ through type II photodynamic processes. This was confirmed through electron spin resonance (ESR) using 5,5-dimethyl-1-pyrroline *N*-oxide (DMPO) and 4-oxo-2,2,6,6-tetramethylpiperidine (TEMP) as capture agents for ·OH and $^1O_2$, respectively. Under light irradiation, characteristic resonance signal peaks of TEMP/$^1O_2$ adducts and DMPO/·OH adducts appeared, indicating the ability of the nanoprobe to generate both ·OH and $^1O_2$ (Figs. 3e and f). Furthermore, the addition of ClO^- to water for laser illumination did not cause characteristic peaks of the capture agents to appear, indicating that the activation of PDT after the ClO^- reaction did not involve the reaction of ClO^- with the captor. Thus, the nanoprobe

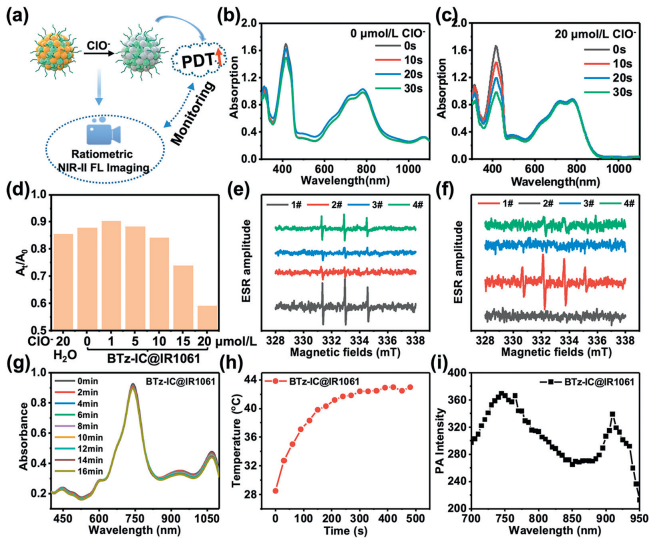

Fig. 3. (a) Diagram of ClO^- activation ratiometric NIR-II fluorescence imaging monitoring activation PDT. (b, c) After incubation with nanoprobe at different concentrations of ClO^-, absorption changes of DPBF at 415 nm before and after light exposure (concentrations of ClO^-: (b) 0 μmol/L, (c) 20 μmol/L)). (d) The absorption ratio of DPBF at 415 nm wavelength after 30 s irradiation and before irradiation after the reaction of nanoparticles with different concentrations of ClO^-. (e, f) The ESR spectra of different groups after exposure to 808 nm using TEMP as the $^1O_2$ scavenger (e) and DMPO as the ·OH catcher (f) (1#: BTz-IC@IR1061 + ClO^- + 808 nm laser, 2#: H_2O + ClO^- + 808 nm laser, 3#: H_2O + 808 nm laser, 4#: BTz-IC@IR1061 + 808 nm laser) (1 W/cm^2, 2 min). (g) Stability of BTz-IC@IR1061 nanoparticles under light conditions (808 nm, 1.0 W/cm^2). (h) Temperature curves of BTz-IC@IR1061 solutions under laser irradiation. (i) Photoacoustic spectra of BTz-IC@IR1061 nanoparticles.

exhibited excellent ClO^- activated PDT and the restoration of fluorescence performance, resulting from the destruction of FRET between BTz-IC and IR1061.

The photostability of the nanoprobe BTz-IC@IR1061 was examined, and even after 16 min of irradiation with an 808 nm laser, the UV spectrum of the nanoprobe remained unchanged, indicating its good photostability (Fig. 3g).

Additionally, the photoacoustic imaging and photothermal capabilities of the nanoprobe were investigated. The nanoprobe generated heat when exposed to 808 nm light, and its photothermal properties remained unaffected after incubation with ClO^-. Moreover, the nanoprobe demonstrated photoacoustic imaging capability, with characteristic peaks of BTz-IC and IR1061 in the spectrum (Figs. 3h and i). These findings laid the foundation for further investigations into the imaging and treatment of tumors using the nanoprobes at both cellular and *in vivo* levels.

To assess the anticancer effect of the BTz-IC@IR1061 nanoprobe *via* PDT, cell-level experiments were conducted. First, the cytotoxicity of the nanoprobes was validated using the cell counting kit-8 (CCK-8) reagent and 4T1 cancer cells. Even at a concentration of up to 100 μg/mL, incubation with BTz-IC@IR1061 for 24 h did not significantly affect cell growth, and cytotoxicity was lower in dark environments. The killing ability of PDT on cells was further confirmed. Cells incubated with GSH and pre-reacted BTz-IC@IR1061 nanoprobe with ClO^- exhibited a 58% cell lethality rate upon 808 nm laser irradiation. However, the groups treated with BTz-IC@IR1061 + 808 nm illumination and BTz-IC@IR1061 + GSH + 808 nm light showed lethality rates of 56% and 0%, respectively. Importantly, neither BTz-IC@IR1061 + GSH nor BTz-IC@IR1061 + ClO^- resulted in significant cell death, indicating that BTz-IC@IR1061, GSH, and ClO^- alone did not cause tumor cell death. These results demonstrated the nanoprobe's ability to activate photodynamic killing of cancer cells (Figs. S9a and b in Supporting information). Next, alive/dead cells staining experiment was employed to study the anticancer activity under irradiation (Fig. S10 in Supporting information), in which live and dead cells were differentiated by calcein acetoxymethyl ester (AM) (green fluorescence) and propidium iodide (PI) (red fluorescence), respectively. Notably, nearly all cells emit red fluorescence (cell death) after treatment of BTz-IC@IR1061 + ClO^- + 808 nm laser, thus indicating the effective ablation of cancer cells under laser irradiation.

The photodynamic effect of the nanoprobe on 4T1 cells was verified by monitoring the production of ROS using 2′,7′-dichlorofluorescein diacetate (DCFH-DA). After BTz-IC@IR1061 + ClO^- + 808 nm light treatment, a large amount of ROS was generated, resulting in strong green fluorescence emission around the nucleus. In contrast, weak green fluorescence was observed in the BTz-IC@IR1061 + 808 nm light group, and no green fluorescence was observed in the ClO^- + 808 nm light group or any group without light. This indicated that the production of ROS was primarily induced by PDT rather than ClO^- or laser irradiation. These findings demonstrated the nanoprobe's ability to generate a significant amount of ROS under light through an activated photodynamic process, effectively targeting cancer cells (Fig. S11 in Supporting information).

Thus, the BTz-IC@IR1061 nanoprobe exhibited promising features for ClO^- activated PDT, demonstrating excellent photostability, photoacoustic imaging, photothermal effects, and the ability to generate ROS for cancer cell killing. These findings supported the potential application of the nanoprobe in the PDT of tumors.

Following the verification of the cytotoxicity of the nanoprobe, its remarkable PDT properties in both solution and cells prompted us to investigate the *in vivo* imaging of cancer. All animal experiments were conducted in accordance with the Guidelines for the Care and Use of Laboratory Animals of Hunan University, and experiments were approved by the Animal Ethics Committee of the College of Biology (Hunan University). We examined the tumor enrichment effect of BTz-IC@IR1061 in a mouse model with 4T1 tumors. Intravenous injection of 200 μL of BTz-IC@IR1061 nanoparticles (2 mg/mL) was performed in BALB/c mice with subcutaneous 4T1 tumors, and photoacoustic and NIR fluorescence images were captured at different time points. As depicted in Fig. S12a (Supporting information), the photoacoustic brightness of the tumor site gradually increased over time, peaking at 8 h after injection (Fig. S12b in Supporting information). Moreover, NIR-induced fluorescence images of mice receiving nanoparticle *via* intravenous injections were collected using a NIR-II fluorescence imager. These images revealed a gradual enhancement of high contrast in the tumor area under 808 nm and 1064 nm excitation (Fig. 4a), accompanied by a time-dependent increase in NIR-II fluorescence signal. Notably, fluorescence intensities in both excitation channels increased over time. Specifically, fluorescence in the tumor area reached its maximum at 4 h under 808 nm excitation, while under 1064 nm excitation, the fluorescence intensity exhibited a pattern of initial increase, followed by a decrease, and then another increase. Additionally, after 4 h of nanoparticle *via* intravenous injections, the fluorescence in the tumor area reached its maximum at 808 nm, whereas fluorescence at 1064 nm was the lowest (Figs. 4b and c). This observation suggests that the nanoprobe, upon initial arrival at the tumor site, was partially activated by ClO^- present within the tumor, and as time progressed, its tumor enrichment increased, resulting in a gradual increase in fluorescence at 1064 nm. The discernible NIR-II fluorescence signal originating from the tumor area indicated that BTz-IC@IR1061 nanoparticles possess effective tumor-targeting capabilities through enhanced permeability and retention rate (EPR) effects.

BALB/c mice with 4T1 tumors (mouse breast cancer) received intratumoral injection of 50 μL of BTz-IC@IR1061 nanoprobe, followed by irradiation with an 808 nm laser for 7 min (0.4 W/cm^2) after 30 min. The results presented in Fig. 4d showed that, follow-

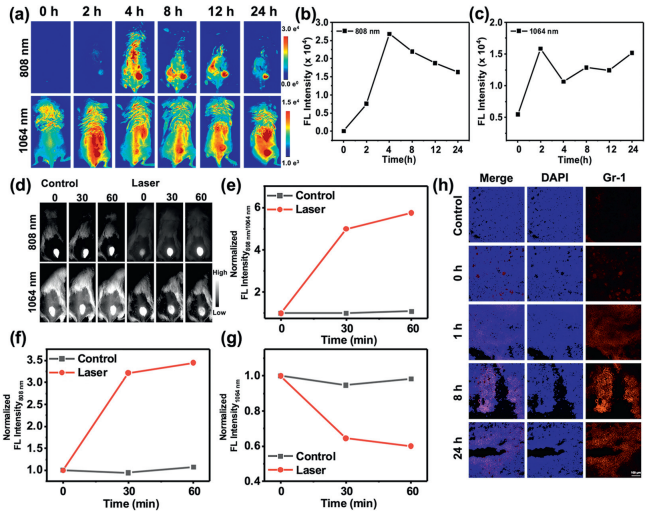

Fig. 4. (a) NIR II fluorescence images of two channels at different time after intravenous injection (i.v.) BTz-IC@IR1061 NPs (Ex: 808 nm, Em > 900 nm; Ex: 1064 nm, Em > 1100 nm). (b) The fluorescence intensity of the 808 nm excitation channel in the tumor region of (a). (c) The fluorescence intensity of the 1064 nm excitation channel in the tumor region of (a). (d) Mice were intratumorally injected with BTz-IC@IR1061 NPs and with different treatment (Control: BTz-IC@IR1061; Laser: BTz-IC@IR1061 + Laser) in different fluorescence channels (Ex: 808 nm, Em > 900 nm; Ex: 1064 nm, Em > 1100 nm). (e) Normalized fluorescence ratio (808 nm/1064 nm) of different groups with different time. (f) Normalized fluorescence intensity curve of different groups with time at 808 nm. (g) Normalized fluorescence intensity curve of different groups with time at 1064 nm. (h) Neutrophil staining of tumor tissues at different times (0, 1, 8, 24 h) after PDT (2-(4-amidinophenyl)−6-indolecarbamidine dihydrochloride (DAPI): λ_{Ex}: 405 nm; Gr-1: λ_{Ex}: 640 nm). Scale bar: 100 μm.

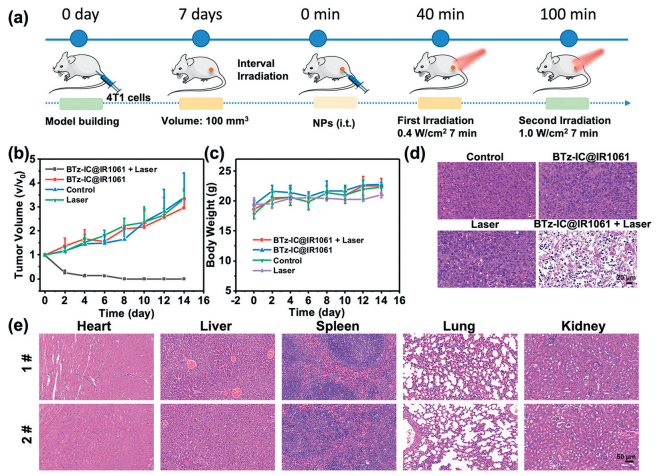

Fig. 5. (a) Timeline of PDT in mice (intratumoral injection (i.t.)). (b) Tumor growth curves of 4T1 tumor mice after different treatments. (c) Body weight change curve of mice in each group. (d) Tumor H&E sections were stained for 24 h in different groups. Scale bar: 20 μm. (e) After 14 days of treatment, H&E sections of major organs were stained in different groups (1#: Control; 2#: BTz-IC@IR1061 NPs + 808 nm laser). Scale bar: 50 μm.

ing 1 h of laser irradiation, fluorescence induced at 1064 nm gradually decreased compared to pre-irradiation levels, while fluorescence induced at 808 nm increased. Conversely, mice that did not undergo laser irradiation exhibited no significant changes in fluorescence signals (Figs. 4f and g). Upon normalization of the fluorescence ratio between 808 nm and 1064 nm, we observed an approximately sixfold increase in the fluorescence ratio after 1 hour of tumor irradiation (Fig. 4e). To investigate the reasons behind this change in fluorescence ratio, we employed a commercial Gr-1 fluorescence probe to assess neutrophil expression in tumors at different time points following irradiation. As illustrated in Fig. 4h, the fluorescence of Gr-1 gradually increased and subsequently decreased in tissue slices at various time intervals post-illumination. This pattern may be attributed to inflammation within the tumor post-irradiation, leading to an increase in neutrophil count, with peak fluorescence intensity observed at 8 h, followed by a decline. Existing literature suggests that an increase in neutrophil count promotes an elevated concentration of ClO^- within tumors. Consequently, the gradual degradation of IR1061 by ClO^- within the tumor likely contributed to the change in fluorescence ratio. Moreover, changes in fluorescence can activate PDT, thereby allowing the monitoring of tumor treatment *via* variations in ratiometric fluorescence.

The biocompatibility and potent photodynamic effects exhibited by BTz-IC@IR1061 nanoparticles *in vitro* motivated us to evaluate their therapeutic efficacy in mice. BALB/c mice with 4T1 subcutaneous tumors were subjected to four treatment conditions: (i) PBS; (ii) 808 nm laser; (iii) BTz-IC@IR1061 nanoparticles; and (iv) BTz-IC@IR1061 nanoparticles + 808 nm laser. As depicted in the timeline depicted in Fig. 5a, after 30 min of intratumoral injection of 50 μL of BTz-IC@IR1061 nanoprobes, the tumor was pre-irradiated for 7 min, followed by a second PDT treatment one hour later. The tumor volume was measured every other day after the treatment. As demonstrated by the tumor growth curve, mice treated with BTz-IC@IR1061 + 808 nm laser exhibited a stronger inhibitory effect, leading to complete tumor disappearance after 14 days of treatment. In contrast, control mice showed progressive tumor growth (Fig. 5b). Furthermore, there were no significant changes in the body weight of all mice in the various treatment groups after 14 days of treatment (Fig. 5c), indicating the effectiveness and high biological safety of PDT for subcutaneous tumors. After 24 h of treatment, the mice were euthanized, and the tumors were subjected to pathological examination. Hematoxylin and eosin (H&E) staining of the tumor sections from group (iv) revealed significant pathological changes compared to the other groups, providing further confirmation of the efficacy of PDT in treating solid tumors (Fig. 5d). Additionally, no notable abnormalities were observed in the major organs following 14 days of treatment, indicating the high biological safety of this administration method (Fig. 5e and Fig. S13 in Supporting information).

In summary, the present study describes the development of a novel ratiometric NIR-II fluorescent organic nanoprobe, designated as BTz-IC@IR1061. This nanoprobe comprises the organic small molecule dye BTz-IC, possessing an A-D-A'-D-A conjugated structure, and the commercial dye IR1061. Notably, BTz-IC can generate both ·OH *via* the type-I photodynamic process and $^1O_2$ *via* the type-II photodynamic process. When assembled into hydrophilic nanoparticles through surfactants, FRET occurs between the two molecules, leading to quenching of the fluorescence and photodynamic activities of BTz-IC. Upon destruction of IR1061 by ClO^-, the fluorescence and PDT of BTz-IC are restored, facilitating proportional BTz-IC fluorescence imaging for monitoring PDT. Furthermore, the first PDT led to infiltration of neutrophils at the tumor site, followed by an increase in HClO concentration, which further led to changes in the ratio of NIR-II fluorescence and the activation of PDT. Besides, the activation of tumor PDT is monitored through the changes of ratiometric NIR-II fluorescence.

Declaration of competing interest

The all authors declare that they have no known competing financial interests or personal relationships that could have appeared to influence the work reported in this paper.

CRediT authorship contribution statement

Baoli Yin: Writing – original draft, Methodology, Investigation, Formal analysis, Data curation, Conceptualization. **Xinlin Liu:** Validation. **Zhe Li:** Validation. **Zhifei Ye:** Writing – review & editing. **Youjuan Wang:** Formal analysis. **Xia Yin:** Project administration, Funding acquisition. **Sulai Liu:** Supervision. **Guosheng Song:** Writing – review & editing, Supervision, Project administration. **Shuangyan Huan:** Project administration, Funding acquisition, Data curation. **Xiao-Bing Zhang:** Project administration, Funding acquisition.

Acknowledgments

This work was supported by the National Natural Science Foundation of China (Nos. 22374040, U21A20287, 21974039, 21890744), the Key Projects of National Natural Science Foundation of China (No. 22234003), the National Key R&D Program of China (No. 2019YFA0210100), and the Fundamental Research Funds for the Central Universities.

Supplementary materials

Supplementary material associated with this article can be found, in the online version, at doi:10.1016/j.cclet.2024.110119.

References

[1] X. Liu, W. Zhan, G. Gao, et al., J. Am. Chem. Soc. 145 (2023) 7918–7930.
[2] D. Li, X. Chen, D. Wang, et al., Biomaterials 283 (2022) 121476.
[3] M. Wang, M. Wu, X. Liu, et al., Adv. Sci. 9 (2022) 2202914.
[4] L. Zhu, S. Lin, W. Cui, et al., Biomater. Sci. 10 (2022) 3624–3636.
[5] Y. Xu, C. Li, J. An, et al., Sci. China Chem. 66 (2023) 155–163.
[6] Y. Xu, C. Li, X. Ma, Y. Sun, Proc. Natl. Acad. Sci. U. S. A. 119 (2022) e2209904119.
[7] Y. Xu, C. Li, S. Lu, et al., Nat. Commun. 13 (2022) 2009.
[8] Z. Zhou, J. Song, R. Tian, et al., Angew. Chem. Int. Ed. 56 (2017) 6492–6496.
[9] P. Sarbadhikary, B. George, H. Abrahamse, Theranostics 11 (2021) 9054–9088.
[10] J. Xie, Y. Wang, W. Choi, et al., Chem. Soc. Rev. 50 (2021) 9152–9201.
[11] V. Nguyen, Z. Zhao, B. Tang, J. Yoon, Chem. Soc. Rev. 51 (2022) 3324–3340.
[12] W. Syu, H. Yu, C. Hsu, et al., Small 8 (2012) 2060–2069.
[13] H. Cho, S. Park, W. Jung, et al., ACS Nano 14 (2020) 15793–15805.
[14] J. Sandland, R. Boyle, Bioconjugate Chem. 30 (2019) 975–993.
[15] H. Benachour, A. Sève, T. Bastogne, et al., Theranostics 2 (2012) 889–904.
[16] S. Li, Q. Zou, Y. Li, et al., J. Am. Chem. Soc. 140 (2018) 10794–10802.
[17] F. Li, Y. Du, J. Liu, et al., Adv. Mater. 30 (2018) 1870264.
[18] K. Ihsanullah, B. Kumar, Y. Zhao, et al., Biomaterials 245 (2020) 119982.
[19] J. Zhang, Y. Zhang, H. Zhang, et al., J. Mater. Chem. B 11 (2023) 4102–4110.
[20] Y. Liu, Y. Li, L. Yu, et al., Anal. Chem. 94 (2022) 811–819.
[21] J. Xiong, J. Chu, W. Fong, C. Wong, D. Ng, J. Am. Chem. Soc. 144 (2022) 10647–10658.
[22] Y. Ichikawa, M. Kamiya, F. Obata, et al., Angew. Chem. Int. Ed. 53 (2014) 6772–6775.
[23] L. Tam, J. Chu, L. He, C. Yang, et al., J. Am. Chem. Soc. 145 (2023) 7361–7375.
[24] E. Han, B. Kwon, D. Yoo, C. Kang, G. Khang, D. Lee, Bioconjug. Chem. 28 (2017) 968–978.
[25] M. Phillipson, P. Kubes, Nat. Med. 17 (2011) 1381–1390.
[26] A. Mantovani, M.A. Cassatella, C. Costantini, S. Jail-lon, Nat. Rev. Immunol. 11 (2011) 519–531.
[27] E. Kolaczkowska, P. Kubes, Nat. Rev. Immunol. 13 (2013) 159–175.
[28] J. Wang, Y. Zhang, E. Archibong, F.S. Ligler, Z. Gu, Adv. Biosyst. 1 (2017) 1700084.
[29] Q. Xu, C. He, C. Xiao, X. Chen, Macromol. Biosci. 16 (2016) 635–646.
[30] S. Klebanoff, J. Leukocyte Biol. 77 (2005) 598–625.
[31] C. Zhang, L. Zhang, W. Wu, et al., Adv. Mater. 31 (2019) 1901179.
[32] O. Soehnlein, S. Steffens, A. Hidalgo, C. Weber, Nat. Rev. Immunol. 17 (2017) 248–261.